How Reliable Is the Ideal Adsorbed Solution Theory for the Estimation of Mixture Separation Selectivities in Microporous Crystalline Adsorbents?

Rajamani Krishna* and Jasper M. van Baten

ACCESS | Metrics & More | Article Recommendations | Supporting Information

ABSTRACT: Microporous crystalline adsorbents such as zeolites and metal−organic frameworks (MOFs) have potential use in a wide variety of separation applications. The adsorption selectivity S_{ads} is a key metric that quantifies the efficacy of any microporous adsorbent in mixture separations. The Ideal Adsorbed Solution Theory (IAST) is commonly used for estimating the value of S_{ads}, with unary isotherms of the constituent guests as data inputs. There are two basic tenets underlying the development of the IAST. The first tenet mandates a homogeneous distribution of adsorbates within the pore landscape. The second tenet requires the surface area occupied by a guest molecule in the mixture to be the same as that for the corresponding pure component. Configurational-bias Monte Carlo (CBMC) simulations are employed in this article to highlight several scenarios in which the IAST fails to provide a quantitatively correct description of mixture adsorption equilibrium due to a failure to conform to either of the two tenets underpinning the IAST. For CO_2 capture with cation-exchanged zeolites and MOFs with open metal sites, there is congregation of CO_2 around the cations and unsaturated metal atoms, resulting in failure of the IAST due to an inhomogeneous distribution of adsorbates in the pore space. Thermodynamic non-idealities also arise due to the preferential location of CO_2 molecules at the window regions of 8-ring zeolites such as DDR and CHA or within pockets of MOR and AFX zeolites. Thermodynamic non-idealities are evidenced for water/alcohol mixtures due to molecular clustering engendered by hydrogen bonding. It is also demonstrated that thermodynamic non-idealities can be strong enough to cause selectivity reversals, which are not anticipated by the IAST.

water and ethanol clustering in DDR
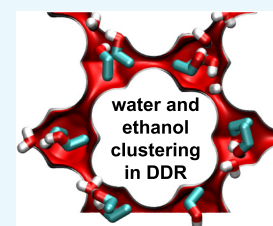
1. INTRODUCTION

Microporous adsorbents such as zeolites and metal−organic frameworks (MOFs) offer energy-efficient alternatives to conventional separation technologies such as distillation. There has been a tremendous upsurge in research on the development of MOFs for a variety of applications such as CO_2 capture and alkene/alkane, alkyne/alkene, and water/alcohol mixture separations. In industrial practice, there are two alternative configurations for utilizing the microporous materials: (i) as crystallites in fixed-bed devices that are operated in transient mode in pressure swing adsorption (PSA) technologies and (ii) as thin perm-selective layers in membrane constructs. A key metric that quantifies the separation performance of both fixed-bed adsorbers and membrane permeation units is the adsorption selectivity S_{ads}. Intracrystalline diffusional influences serve to either enhance or diminish the separation efficacy dictated by mixture adsorption equilibrium. For n-component mixture adsorption, the selectivity of guest constituent i with respect to another guest constituent j in that mixture, $S_{ads, ij}$, is defined by

$$S_{ads,ij} = \frac{q_i/q_j}{f_i/f_j} = \frac{q_i/q_j}{y_i/y_j}$$

(1)

where q_i and q_j are the molar loadings of the constituents i and j in the adsorbed phase in equilibrium, respectively, with the bulk fluid phase mixture having partial fugacities f_i and f_j and mole fractions $y_i = f_i/f_t$; $f_t = (\sum_{k=1}^{n} f_k)$. For the estimation of the component loadings and selectivity $S_{ads, ij}$, it is a common practice to use the Ideal Adsorbed Solution Theory (IAST)[1,2] that requires the unary isotherm data as inputs. The IAST approach has been used in a number of published works for evaluating and ranking microporous crystalline adsorbents for separating a wide variety of mixtures, including CO_2/CH_4,[3,4] CO_2/N_2,[3,5] CO_2/H_2,[6,7] SO_2/CO_2/N_2,[8] C_2H_2/C_2H_4,[9−11] C_2H_2/CO_2,[12] C_2H_4/C_2H_6,[13−17] C_3H_4/C_3H_6,[18−20] C_3H_6/C_3H_8,[16,21] Xe/Kr,[22,23] water/alcohol,[24−27] pentane isomers,[28] hexane isomers,[29−31] xylene isomers,[32−34] and ethylbenzene/styrene.[35,36]

Of these cited references, the validity of the use of the IAST for providing quantitatively accurate estimates of selectivities
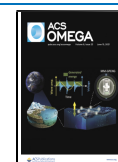
has been established by resorting to configurational-bias Monte Carlo (CBMC) simulations in the following limited number of cases: C_2H_2/C_2H_4 in ZUL-100 and ZUL-200,[11] hexane isomers in $Fe_2(BDP)_3$[30] and ZIF-77,[31] and xylene isomers in MAF-X8.[34]

Despite the widespread usage of the IAST, a limited number of investigations have found that IAST estimates of component loadings for mixture adsorption are not in quantitative agreement with experimental data. These studies include the adsorption of CO_2/N_2,[37] CO_2/CH_4,[38−41] CO_2/C_3H_8,[42−44] CO_2/C_2H_4,[45−47] CO_2/H_2S,[48] and H_2S/C_3H_8[48] mixtures in cation-exchanged zeolites such as NaX (commonly known by its trade name 13X), LTA-5A, ZSM-5, and H-MOR.

The primary objective of this article is to investigate the reliability of IAST estimates of mixture adsorption equilibrium. We aim to highlight a variety of scenarios that would enable researchers to anticipate the possibility of the failure of the IAST to provide quantitative estimates of the component loadings in the adsorbed phase. To meet with the objectives, we resort to configurational-bias Monte Carlo (CBMC) simulations of the unary and mixture adsorption equilibrium for a wide variety of guest/host combinations. The CBMC simulations are performed using the methodology that is firmly established in the literature; details are provided in the Supporting Information accompanying this publication, which also includes (a) structural details of host materials, (b) CBMC data for unary and mixture adsorption, and (c) unary isotherm data fits.

2. RESULTS AND DISCUSSION

2.1. The IAST and Its Prescriptions. In the Myers−Prausnitz development of the IAST,[1] the partial fugacities in the bulk fluid mixture are related to the mole fractions x_i in the adsorbed phase mixture

$$x_i = q_i/q_t; \quad q_t = q_1 + q_2 + ... + q_n; \quad i = 1, 2, ..., n \tag{2}$$

by the analogue of Raoult's law for vapor−liquid equilibrium, i.e.,

$$f_i = P_i^0 x_i; \quad i = 1, 2, ..., n \tag{3}$$

where P_i^0 is the pressure for sorption of every component i, which yields the same spreading pressure π for each of the pure components, as that for the mixture:

$$\frac{\pi A}{RT} = \int_0^{P_1^0} \frac{q_1^0(f)}{f} df = \int_0^{P_2^0} \frac{q_2^0(f)}{f} df$$
$$= \int_0^{P_3^0} \frac{q_3^0(f)}{f} df = ... \tag{4}$$

In eq 4, A represents the surface area per kg of framework, and $q_i^0(f)$ is the pure component adsorption isotherm; the superscript 0 is used to emphasize that $q_i^0(f)$ relates the pure component loading to the bulk fluid fugacity. Since the surface area A is not directly accessible from experimental data, the surface potential,[40,43] $\frac{\pi A}{RT} \equiv \Phi$, with the unit mol kg^{-1}, serves as a convenient and practical proxy for the spreading pressure π; the surface potential has also been termed the adsorption potential in several recent publications.[49−52]
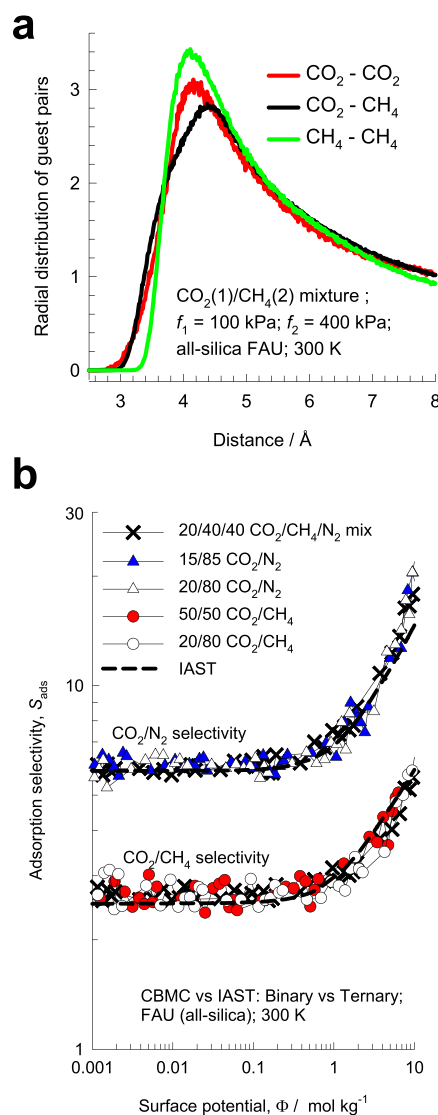
Figure 1. (a) Radial distribution of guest pairs determined from CBMC simulations for the adsorption of CO_2/CH_4 mixtures in all-silica FAU zeolite at 300 K and total fugacity f_t = 500 kPa and y_1 = 0.2. (b) CBMC data for adsorption selectivity for 50/50 CO_2/CH_4, 20/80 CO_2/CH_4, 15/85 CO_2/N_2, 20/80 CO_2/N_2, and 20/40/40 $CO_2/CH_4/N_2$ mixtures in all-silica FAU. The x-axis represents the surface potential Φ. The dashed lines are the IAST estimations. All calculation details and input data are provided in the Supporting Information accompanying this publication.

For multicomponent mixture adsorption, each of the equalities on the right side of eq 4 must be satisfied. These constraints may be solved using a suitable equation solver to yield the set of values of $P_1^0, P_2^0, P_3^0, ..., P_n^0$, all of which satisfy eq 4. The corresponding values of the integrals using P_i^0 as upper limits of integration must yield the same value of the surface potential Φ for each component; this ensures that the obtained solution is the correct one.

The adsorbed phase mole fractions x_i are then determined from

$$x_i = f_i/P_i^0; \quad i = 1, 2, ..., n \tag{5}$$

The applicability of eq 5 mandates that all of the adsorption sites within the microporous material are equally accessible to each of the guest molecules, implying a homogeneous
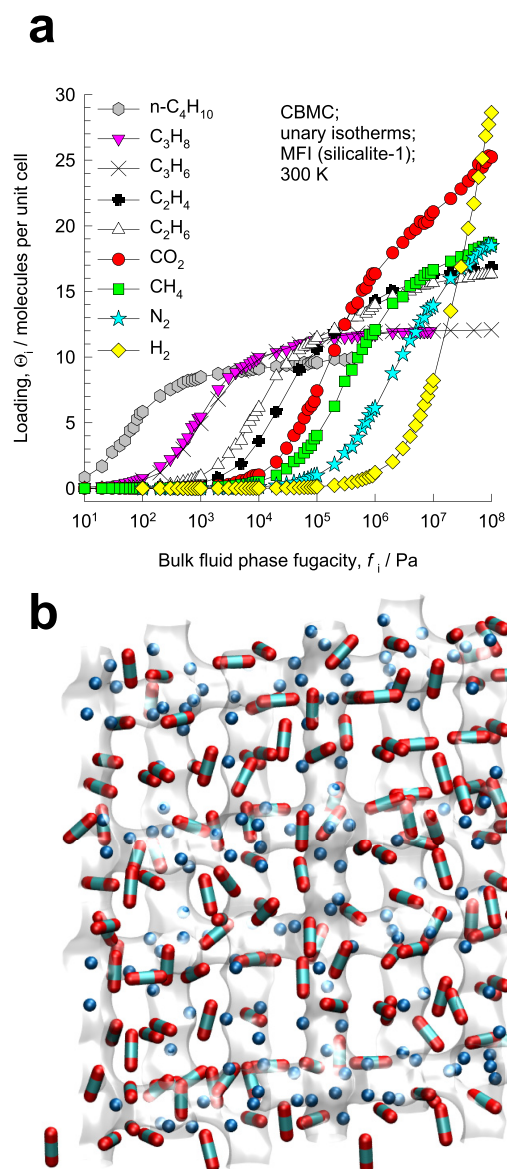
a

b

Figure 2. (a) CBMC simulations of unary isotherms for light gaseous molecules H_2, N_2, CO_2, CH_4, C_2H_4, C_2H_6, C_3H_6, C_3H_8, and n-C_4H_{10} in MFI zeolite at 300 K. (b) Computational snapshots showing the location of CO_2 and CH_4 for binary mixture adsorption in MFI.

distribution of guest adsorbates within the pore landscape, with no preferential locations of any guest species.

In view of eqs 2 and 5, we rewrite eq 1 as the ratio of the sorption pressures

$$S_{ads,ij} = P_j^0 / P_i^0 \qquad (6)$$

Applying the restriction specified by eq 4, it follows that $S_{ads, ij}$ is uniquely determined by the surface potential Φ. It is important to note that eq 6 is valid irrespective of the total number of components in the mixture. In other words, the presence of component 3 in the ternary mixture has no direct influence on the adsorption selectivity $S_{ads,12} = P_2^0/P_1^0$ for the 1−2 pair, except for the fact that the surface potential Φ that satisfies eq 4 is altered due to the presence of component 3.

A further key assumption of the IAST is that the adsorption enthalpies and surface areas of the adsorbed molecules do not change upon mixing with other guests. If the total mixture

loading is q_t, the area covered by the adsorbed mixture is $\frac{A}{q_t}$ with the unit m^2 (mole mixture)$^{-1}$. Therefore, the assumption of no surface area change due to mixture adsorption translates as $\frac{A}{q_t} = \frac{Ax_1}{q_1^0(P_1^0)} + \frac{Ax_2}{q_2^0(P_2^0)} + \cdots + \frac{Ax_n}{q_n^0(P_n^0)}$; the total mixture loading is $q_t = q_1 + q_2 + \ldots + q_n$, which is calculated from

$$\frac{1}{q_t} = \frac{x_1}{q_1^0(P_1^0)} + \frac{x_2}{q_2^0(P_2^0)} + \ldots + \frac{x_n}{q_n^0(P_n^0)} \qquad (7)$$

in which $q_1^0(P_1^0)$, $q_2^0(P_2^0)$, ..., $q_n^0(P_n^0)$ are determined from the unary isotherm fits, using the sorption pressures for each component P_1^0, P_2^0, P_3^0, ..., P_n^0, that are available from the solutions to eq 4. The occurrence of molecular clustering and hydrogen bonding should be expected to invalidate the applicability of eq 7 because the surface area occupied by a molecular cluster is different from that of each of the unclustered guest molecules in the adsorbed phase.

The ratio of the total mixture loading, q_t, to the saturation capacity of the mixture, $q_{sat, mix}$, is the fractional pore occupancy, θ, which is relatable to Φ as follows (see the Supporting Information for the complete derivation)

$$\theta \equiv q_t / q_{sat,mix} = 1 - \exp(-\Phi / q_{sat,mix}) \qquad (8)$$

where the saturation capacity $q_{sat, mix}$ is calculated from the saturation capacities of the constituent guests

$$\frac{1}{q_{sat,mix}} = \sum_{k=1}^{n} \frac{x_k}{q_{k,sat}} \qquad (9)$$

The surface potential Φ is therefore also interpretable as a proxy for the pore occupancy.

Armed with these concepts, let us compare the CBMC simulation data for mixture adsorption with the IAST predictions. Further details of the CBMC simulations (force fields used and host structures) and IAST (unary isotherm data fits) are provided in the Supporting Information.

2.2. Homogeneously Distributed Guests: Fulfilling the IAST Prescription. A quantitative procedure to verify the IAST precept of homogeneous distribution of guest adsorbates within the pore space is to perform CBMC simulations to determine the spatial locations of the guest molecules and to determine the intermolecular distances. As an illustration, we consider CO_2/CH_4 mixture adsorption in all-silica FAU zeolite with a total fugacity $f_t = 500$ kPa and $y_1 = 0.2$ at 300 K. FAU zeolite has a large "open" structure that consists of cages with a volume of 786 Å^3, separated by 12-ring windows with a size of 7.4 Å. By sampling a total of 10^5 simulation steps, the radial distribution of the separation distances between the molecular pairs CO_2–CO_2, CO_2–CH_4, and CH_4–CH_4 were determined. The data on the distances between the molecular pairs CO_2–CO_2, CO_2–CH_4, and CH_4–CH_4 are shown in Figure 1a; such plots are commonly termed radial distribution functions (RDFs). We note that the peaks occur at practically the same intermolecular distances. This indicates that there are no congregation or segregation effects and that the guest molecules are homogeneously distributed within the pore landscape, adequately fulfilling the precept of the IAST. Consequently, we should expect the IAST to provide a good quantitative description of CO_2/CH_4 mixture adsorption in all-silica FAU zeolite. As confirmation, Figure 1b presents CBMC data for CO_2/CH_4, and CO_2/N_2 adsorption selectivities for 50/50 CO_2/CH_4, 20/80 CO_2/CH_4, 15/85 CO_2/N_2, 20/80
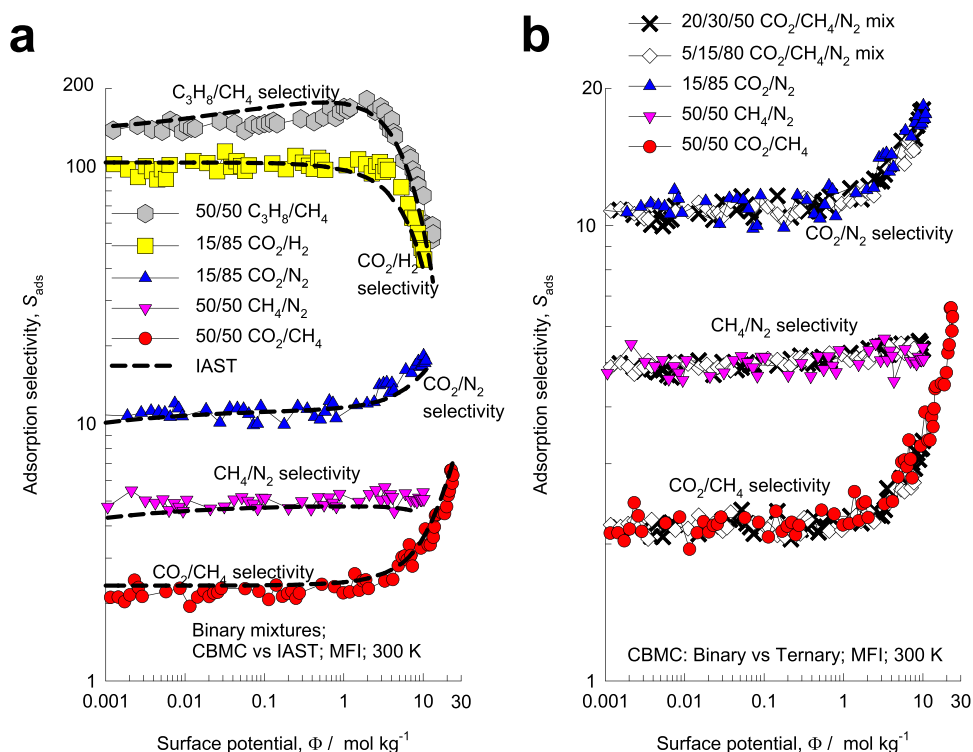
Figure 3. (a) CBMC simulations (indicated by symbols) of the adsorption selectivity S_{ads} for five different binary mixtures: CO_2/CH_4, CO_2/N_2, CH_4/N_2, CO_2/H_2, and C_3H_8/CH_4 in MFI zeolite at 300 K. The dashed lines are the IAST calculations for corresponding S_{ads} values using the dual-site Langmuir−Freundlich fits of unary isotherms. (b) Comparison of CO_2/CH_4, CO_2/N_2, and CH_4/N_2 adsorption selectivities determined from binary mixtures, with the corresponding values in two different ternary mixtures: $5/15/80$ $CO_2/CH_4/N_2$ and $20/30/50$ $CO_2/CH_4/N_2$. The x-axes represent the surface potential Φ. All calculation details and input data are provided in the Supporting Information accompanying this publication.

CO_2/N_2, and $20/40/40$ $CO_2/CH_4/N_2$ mixtures in all-silica FAU. The CO_2/CH_4 and CO_2/N_2 selectivities are uniquely determined by the surface potential Φ, irrespective of the composition of the bulk fluid phase mixture and the presence of the third component. The IAST estimations, shown by the dashed lines, are in good agreement with the CBMC-simulated values of S_{ads}.

Let us turn to mixture adsorption in MFI zeolite, a host structure in which the guest molecules are more strongly constrained. MFI (also called silicalite-1) has a topology consisting of a set of intersecting straight channels and zig-zag (or sinusoidal) channels with sizes of 5.4 Å × 5.5 Å and 5.4 Å × 5.6 Å. The IAST prescription demanding the homogeneous distribution of guest molecules within MFI zeolite is fulfilled only for light gaseous guest molecules such as H_2, N_2, CO_2, CH_4, C_2H_4, C_2H_6, C_3H_6, C_3H_8, and n-C_4H_{10}. These light gaseous guests can locate anywhere along the straight channels and zig-zag channels, and there are no perceptible isotherm inflections, as evidenced in the unary isotherms in Figure 2a. The saturation capacities follow the hierarchy H_2 > CO_2 > N_2 ≈ CH_4 > C_2H_4 ≈ C_2H_6 > C_3H_6 ≈ C_3H_8 > n-C_4H_{10}. Figure 2b shows computational snapshots for the adsorption of CO_2 and CH_4 within the intersecting channel topology of MFI zeolite. It is noticeable that neither guest species show any preferential location and there is no visual indication of segregated adsorption. The Coulombic interactions of CO_2 with the negatively charged oxygen atoms in the zeolite framework are not strong enough to cause segregation between CO_2 and CH_4. We should therefore expect the mixture adsorption characteristics to be adequately well described by the IAST.

The IAST calculations for the adsorption selectivity S_{ads} for five different binary mixtures CO_2/CH_4, CO_2/H_2, CO_2/N_2, CH_4/N_2, and C_3H_8/CH_4 are compared with the corresponding S_{ads} values determined from CBMC simulations in Figure 3a. For all five mixtures, the IAST estimations are in good agreement with the CBMC-simulated data, plotted as a function of the surface potential Φ. For CO_2/CH_4 and CO_2/N_2 mixtures, the S_{ads} increases as pore saturation conditions are approached, i.e., Φ > 10 mol kg^{-1}; θ > 0.5, because of entropy effects that favor the guest CO_2 with the higher saturation capacity (cf. Figure 2a); the explanation of entropy effects is provided in the published literature.[33,53] For CO_2/H_2 and C_3H_8/CH_4 mixtures, the S_{ads} decreases as pore saturation conditions are approached because entropy effects favor the smaller guests H_2 and CH_4, respectively, that have significantly higher saturation capacities. For CH_4/N_2 mixtures, the S_{ads} is practically independent of occupancy because the saturation capacities of CH_4 and N_2 are nearly the same, as evidenced in Figure 2a.

Figure 3b presents a comparison of CO_2/CH_4, CO_2/N_2, and CH_4/N_2 adsorption selectivities determined from binary mixtures in MFI, with the corresponding values determined from CBMC simulations using two different ternary mixtures: $5/15/80$ $CO_2/CH_4/N_2$ and $20/30/50$ $CO_2/CH_4/N_2$. Each of the three selectivities shows a unique dependence on Φ, as prescribed by eqs 5 and 6. In other words, the presence of component 3 in the ternary mixture has no direct influence on the adsorption selectivity for the 1−2 pair other than via Φ, as is anticipated on the basis of the development of the IAST.

Results analogous to those presented in Figures 1b and 3b, demonstrating the unique dependence of S_{ads} on Φ, and the
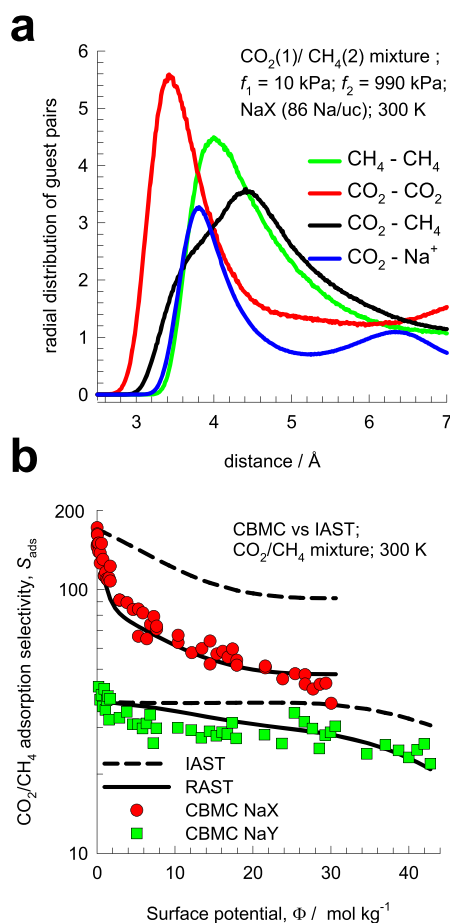
Figure 4. (a) Radial distribution of guest pairs determined from CBMC simulations for the adsorption of CO_2/CH_4 mixtures in NaX zeolite at 300 K and total fugacity f_t = 1 MPa, and y_1 = 0.01. (b) Comparison CO_2/CH_4 adsorption selectivities determined from CBMC simulations for NaY (138 Si, 54 Al, 54 Na^+, and Si/Al = 2.56) and NaX (106 Si, 86 Al, 86 Na^+, and Si/Al = 1.23) zeolites at 300 K. The CBMC-simulated values (indicated by symbols) are compared with RAST (continuous solid lines) and IAST (dashed lines) estimates. All calculation details and input data are provided in the Supporting Information accompanying this publication.

concomitant accuracy of IAST estimates are found for (i) $CO_2/CH_4/N_2$ mixture adsorption in ISV that has intersecting channel structures of 6 Å (see Figure S28), (ii) $CO_2/CH_4/N_2$ mixture adsorption in all-silica LTA zeolite that has cages separated by 4.11 Å × 4.47 Å 8-ring windows (see Figure S77), (iii) adsorption of ternary and quinary mixtures of hexane isomers in Mg_2(dobdc), which has 1D hexagonal channels of 11 Å (see Figure S102a), and (iv) adsorption of ternary and quinary mixtures of hexane isomers in Co(BDP), which has 1D square channels of 10 Å (see Figure S102b). In all these cases, the IAST prescription is met because the guest molecules are homogeneously distributed within the pore landscape, allowing the guest species to compete equitably with one another.

2.3. Congregation of Charged Guests around Cations.

Let us consider CO_2/CH_4 mixture adsorption in cation-exchanged NaX zeolite that has the same pore topology as FAU zeolite; per unit cell NaX zeolite has 106 Si, 86 Al, and 86 Na^+ with Si/Al = 1.23. Figure 4a presents the RDF data determined from CBMC simulations. If we compare the first peaks, it is noteworthy that the CO_2-CO_2 and CO_2-Na^+ pairs are close together, indicating that the major proportion of CO_2

congregates around the cations. A further point to note is that the CO_2-CH_4 separation distance is significantly larger than the CO_2-CO_2 and CH_4-CH_4 separation distances. This implies that the CH_4 molecules face less severe competitive adsorption with CO_2 than is anticipated by the IAST. Consequently, as seen in Figure 4b, the values of S_{ads} estimated by the IAST are significantly higher, by about a factor of two, than those determined by CBMC. Also shown in Figure 4b are the CBMC data for CO_2/CH_4 mixture adsorption in NaY zeolite (138 Si, 54 Al, 54 Na^+, and Si/Al = 2.56); the IAST estimates are also in excess of the CBMC data, but the departures are less than that experienced with NaX because congregation effects are reduced due to the presence of fewer cations in NaY. Of course, in the total absence of cations, the IAST estimates are in excellent agreement with CBMC data, as already witnessed in Figure 1b.

The inhomogeneous distribution of adsorbates is a common feature of mixtures of charged and neutral guests in cation-exchanged zeolites. Figure 5a shows the RDF data for CO_2/C_3H_8 mixture adsorption in NaX zeolite. The $CO_2-C_3H_8$ separation distance is significantly higher than between the CO_2-CO_2 and CO_2-Na^+ pairs, indicating that C_3H_8 experiences reduced competition with CO_2 partners. The consequences of this reduced competition is reflected by the CBMC data for $CO_2(1)/C_3H_8(2)$ mixture adsorption in three different CBMC campaigns: (i) equimolar mixtures, $y_1 = y_2 = 0.5$, with varying $f_t = f_1 + f_2$, (ii) f_t = 1 MPa with varying y_1, and (iii) f_t = 50 kPa with varying y_1. The assumption of an ideal adsorbed mixture anticipates all three data sets to follow a unique $S_{ads} - \Phi$ dependence, as shown by the dashed line in Figure 5b. However, the CBMC data (indicated by symbols) show that the $CO_2(1)/C_3H_8(2)$ adsorption selectivity S_{ads} does not follow a unique dependence on Φ.

To quantify non-ideality effects and departures from the IAST, we need to abandon Raoult's law assumption in eq 3 and introduce activity coefficients γ_i

$$\gamma_i = f_i / x_i P_i^0; \qquad i = 1, 2 \ldots, n \tag{10}$$

Figure 5c presents the activity coefficients calculated from the CBMC data for campaign (i) for equimolar mixtures of CO_2 and C_3H_8 with varying f_t. As $\Phi \rightarrow 0$, both activity coefficients tend to unity $\gamma_i \rightarrow 1$; this corresponds with the Henry regime of adsorption. In other words, at vanishing small values of pore occupancy, non-ideality effects can be ignored, as should be expected. With increasing pore occupancy, the activity coefficient of C_3H_8 steadily decreases below unity, whereas the activity coefficient of CO_2 remains close to unity over the entire range of Φ values.

Figure 5d presents the activity coefficients calculated from the CBMC data for campaign (ii) with f_t = 1 MPa and varying bulk fluid mixture composition; in this campaign, the variation of Φ is minimal and falls in the range 24 < Φ < 30 mol kg^{-1}. Both activity coefficients are strongly dependent on the composition of the adsorbed phase mixture, x_1, and satisfy the requirement $x_i \rightarrow 1$; $\gamma_i \rightarrow 1$.

Following the approaches of Myers, Talu, and Sieperstein,[43,48,54] we model the excess Gibbs free energy for binary mixture adsorption as follows

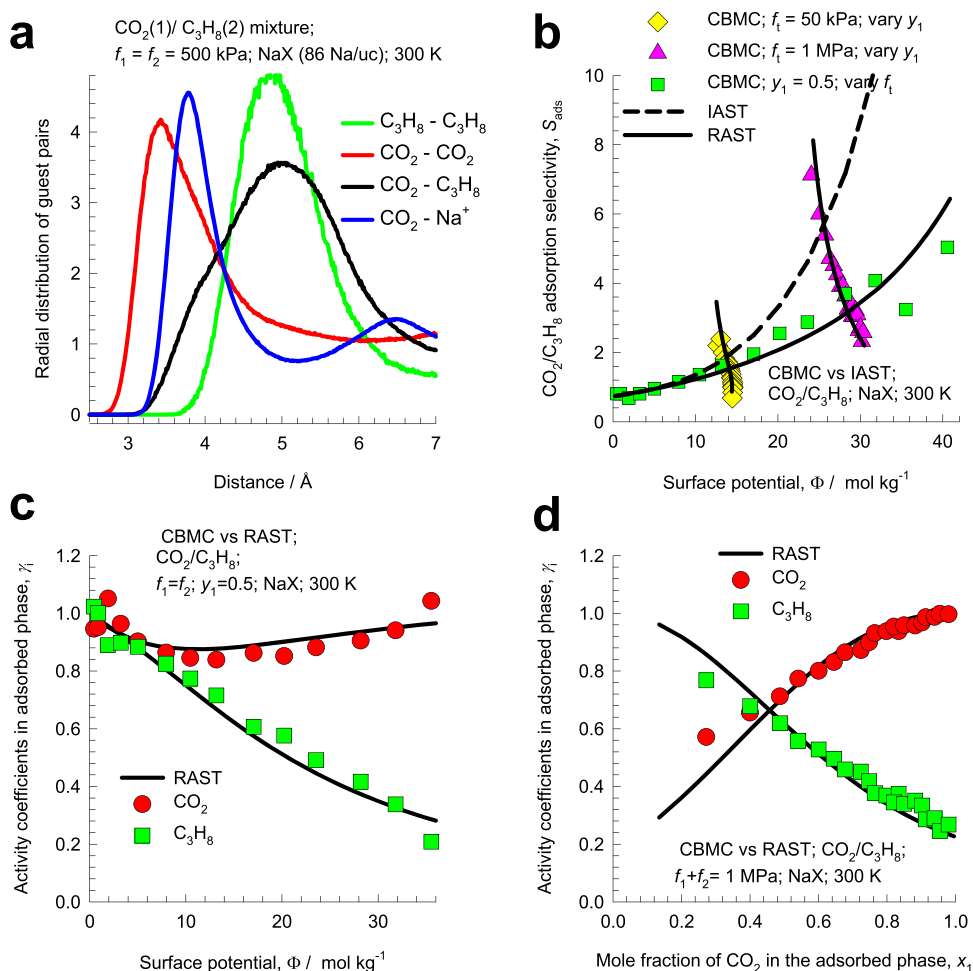$$\frac{G^{excess}}{RT} = x_1 \ln(\gamma_1) + x_2 \ln(\gamma_2) \tag{11}$$

Figure 5. (a) Radial distribution of guest pairs determined from CBMC simulations for the adsorption of CO_2/C_3H_8 mixtures in NaX zeolite at 300 K and total fugacity $f_t = 1$ MPa and $y_1 = 0.5$. (b) Adsorption selectivity S_{ads} for $CO_2(1)/C_3H_8(2)$ mixture adsorption in NaX zeolite at 300 K for three different CBMC campaigns, plotted as a function of the surface potential Φ: (i) constant composition $y_1 = 0.5$ with varying $f_t = f_1 + f_2$, (ii) $f_t = 1$ MPa with varying composition y_1, and (iii) $f_t = 50$ kPa with varying y_1. The CBMC-simulated values (indicated by symbols) are compared with RAST (continuous solid lines) and IAST (dashed lines) estimates. (c) Activity coefficients for $CO_2(1)$ and $C_3H_8(2)$, determined from campaign (i). (d) Activity coefficients for $CO_2(1)$ and $C_3H_8(2)$ determined from campaign (ii). The continuous solid lines in panels (b) and (c) are RAST/Margules model calculations. All calculation details and input data are provided in the Supporting Information accompanying this publication.

For the calculation of the total mixture loading $q_t = q_1 + q_2$, we need to replace eq 7 by

$$\frac{1}{q_t} = \frac{x_1}{q_1^0(P_1^0)} + \frac{x_2}{q_2^0(P_2^0)} + \left(\frac{1}{q_t}\right)^{excess} \tag{12}$$

The excess reciprocal loading for the mixture can be related to the partial derivative of the Gibbs free energy with respect to the surface potential at constant composition

$$\left(\frac{1}{q_t}\right)^{excess} = \left.\frac{\partial\left(\frac{G^{excess}}{RT}\right)}{\partial\Phi}\right|_{T,x} \tag{13}$$

For quantitative modeling of the data on activity coefficients, a variety of models such as regular solution,[43] Wilson,[50,51,55] NRTL,[56] SPD,[48] and Margules[52,57] have been used. For example, the Margules model takes the following form

$$\ln(\gamma_1) = x_2^2(A_{12} + 2(A_{21} - A_{12})x_1)(1 - \exp(-C\Phi))$$

$$\ln(\gamma_2) = x_1^2(A_{21} + 2(A_{12} - A_{21})x_2)(1 - \exp(-C\Phi)) \tag{14}$$

In eq 14, C is a constant with the unit kg mol^{-1}. The introduction of $(1 - \exp(-C\Phi))$ imparts the correct limiting behaviors for the activity coefficients in the Henry regime: $\Phi \to 0$; $\gamma_i \to 1$. As pore saturation conditions are approached, this correction factor tends to unity: $(1 - \exp(-C\Phi)) \to 1$.

Combining eqs 11–14, we derive

$$\frac{1}{q_t} = \frac{x_1}{q_1^0(P_1^0)} + \frac{x_2}{q_2^0(P_2^0)}$$
$$+ x_1 x_2[A_{12}x_2 + A_{21}x_1]C\exp(-C\Phi) \tag{15}$$

The parameters A_{12}, A_{21}, and C can be fitted to match the CBMC data on activity coefficients; the fitting procedure is detailed in the Supporting Information accompanying this publication. The continuous solid lines in Figure 5c,d are calculations following the Real Adsorbed Solution Theory
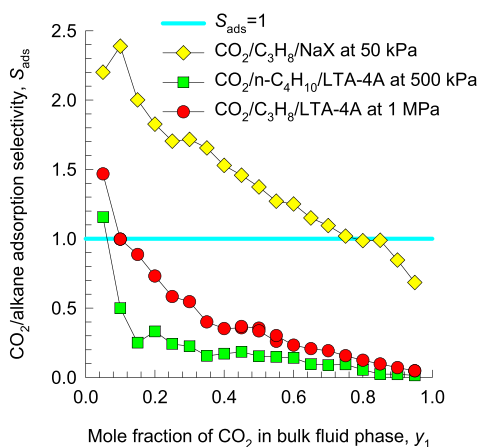
Figure 6. CBMC simulation data for CO_2/alkane selectivities determined from three different CBMC campaigns: (i) $CO_2(1)$/$C_3H_8(2)$ mixture adsorption in NaX with f_t = 50 kPa and varying y_1, (ii) $CO_2(1)$/$C_3H_8(2)$ mixture adsorption in LTA-4A with f_t = 1 MPa and varying y_1, and (iii) $CO_2(1)$/n-$C_4H_{10}(2)$ mixture adsorption in LTA-4A with f_t = 500 kPa and varying y_1. The CO_2/alkane selectivity values in each case are plotted against the mole fraction in the bulk fluid mixture, y_1. All calculation details and input data are provided in the Supporting Information accompanying this publication.

(RAST) with fitted Margules parameters $A_{12} = -3.082$, $A_{21} = -2.170$, and $C = 0.038$ kg mol^{-1}.

With the introduction of activity coefficients, eq 6 needs to be replaced by the more generalized expression for the adsorption selectivity for the i–j pair

$$S_{\text{ads},ij} = \frac{P_j^0 \gamma_j}{P_i^0 \gamma_i} \tag{16}$$

Equations 14 and 16 imply that the $S_{\text{ads}, ij}$ depends on both Φ and the composition of the adsorbed mixture; this point is underscored in the RAST calculations (indicated by the continuous solid lines) of the selectivity for the three campaigns in Figure 5b. An important consequence of this complex dependence is the occurrence of selectivity reversal phenomena. Figure 6 presents CBMC data on the CO_2/C_3H_8 and CO_2/n-C_4H_{10} selectivities for cation-exchanged zeolites NaX and LTA-4A; in the simulations, the total mixture fugacity f_t is maintained at a fixed value. With increasing proportion of CO_2 in the bulk fluid mixture, selectivity reversals in favor of the alkane occur; all such reversals are not anticipated by the IAST (see Figures S69, S75, S76, and S86). Experimental evidence of such selectivity reversals, attributable to congregation of CO_2 around cations, has been reported for CO_2/C_3H_8[42−44] and CO_2/C_2H_4[45] in cation-exchanged zeolites.

For the adsorption of the CO_2-bearing mixture in Mg_2(dobdc), the preponderance of CO_2 around the unsaturated Mg^{2+} sites causes quantitative failure of the IAST; see CBMC data in Figures S95 and S96.

Other examples of the failure of the IAST, along with alternative approaches to RAST modeling of non-idealities, are available in the literature.[2,58−62]

2.4. Preferential Location of Guests at Channel Intersections of MFI Zeolite.
Due to configurational considerations, branched alkanes prefer to locate at the channel intersections of MFI zeolite because of the extra "leg room" that is available here. An extra "push" is required to locate these molecules within the channel interiors. This extra
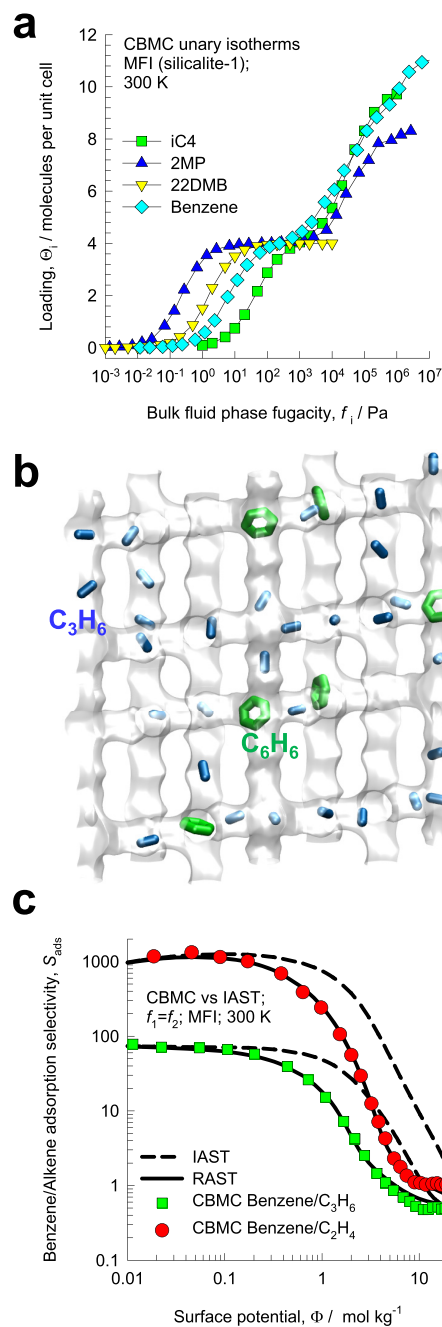

Figure 7. (a) CBMC simulations of unary isotherms for branched alkanes and benzene in MFI zeolite at 300 K. (b) Computational snapshots showing the location of guest molecules for $C_3H_6(1)$/benzene(2) mixture adsorption in MFI zeolite at 300 K. (c) Adsorption selectivity S_{ads} for benzene/C_2H_4 and benzene/C_3H_6 mixtures in MFI zeolite, plotted as a function of the surface potential Φ. The CBMC-simulated values (indicated by symbols) are compared with RAST (continuous solid lines) and IAST (dashed lines) estimates. All calculation details and input data are provided in the Supporting Information accompanying this publication.

push results in an inflection in the pure component isotherms at a loading of four molecules per unit cell because per unit cell of MFI, there are four channel intersection sites;[63−66] see Figure 7a. Cyclic hydrocarbons, such as cyclohexane, benzene, and ethylbenzene, also prefer to locate at the intersections; the unary isotherm for benzene also exhibits a strong inflection at a loading of four molecules per unit cell (cf. Figure 7a). For
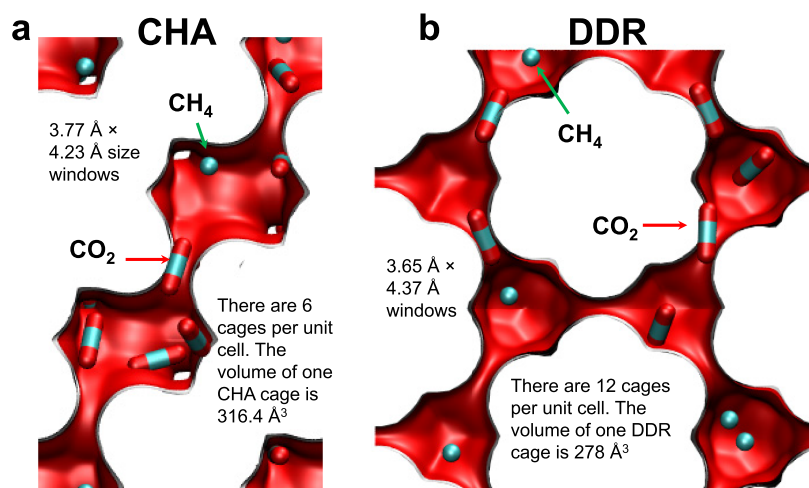
Figure 8. Computational snapshots for $CO_2(1)/CH_4(2)$ mixture adsorption in (a) CHA and (b) DDR zeolites at 300 K.

$C_3H_6(1)$/benzene(2) mixture adsorption in MFI, the computational snapshots in Figure 7b clearly show that the aromatics are exclusively located at the channel intersections, whereas the linear propene can locate anywhere along either the straight or zig-zag channels. Figure 7c plots the CBMC data for adsorption selectivity S_{ads} of $C_2H_4(1)$/benzene(2) and $C_3H_6(1)$/benzene(2) mixtures as functions of Φ. For both mixtures, the IAST (indicated by the dashed lines) significantly overestimates the S_{ads} value in favor of benzene, except for the limiting case of low pore occupancy $\Phi \rightarrow 0$, $\theta \rightarrow 0$. The IAST calculation assumes that alkene molecules (C_2H_4 or C_3H_6) compete with all of the benzene molecules, making no allowance for segregation and preferential adsorption of benzene at the intersections. Due to segregation effects, the competition faced by alkene molecules within the channels is lower than that in the entire pore space. In other words, the IAST anticipates a stiffer competition between benzene and alkenes as it assumes a uniform distribution of adsorbates; consequently, the separation selectivity is overestimated. Due to the preferential location of benzene at the intersections, some alkene molecules are farther removed from benzene and suffer diminished competition.

A further point to be noted is that the benzene/alkene selectivity reduces significantly with increasing values of Φ; this reduction in S_{ads} is a direct consequence of entropy effects that favor alkene because of significantly higher saturation capacity. The CBMC data for C_3H_6/benzene mixtures and entropy effects are strong enough to cause selectivity reversals in favor of propene, for $\Phi > 5$ mol kg^{-1}, corresponding to $\theta > 0.93$. Such selectivity reversal is not quantitatively matched by the IAST; the use of the RAST is necessary for a good quantitative description of $S_{ads} - \Phi$ characteristics.

For precisely analogous reasons, adsorption of C_3H_8/iso-C_4H_{10}, n-C_4H_{10}/iso-C_4H_{10}, and n-hexane/2-methylpentane mixtures in MFI zeolite shows significant deviations from IAST estimates of component loadings and selectivities; see Figures S19–S25 of the Supporting Information.

2.5. Preferential Location of CO_2 at Window Regions of Cage-Type Zeolites. For the separation of CO_2 from gaseous mixtures with CH_4, cage-type zeolites such as CHA, DDR, LTA, and ERI are of practical interest;[67−69] these materials consist of cages separated by narrow windows in the 3.3−4.5 Å range. For adsorption of CO_2/CH_4 mixtures, CBMC simulations[67] show that the window regions of cage-

type zeolites have a significantly higher proportion of CO_2 than within the cages; see computational snapshots in Figure 8 for (a) CHA and (b) DDR zeolites.

In Figure 9a, the CBMC-simulated values of the adsorption selectivity S_{ads} for CO_2/CH_4 mixture adsorption in CHA, determined from three different CBMC campaigns, are plotted as a function of Φ. For all three sets of CBMC data, the IAST calculations overestimate the values of S_{ads} because the competition faced by CH_4, which locates predominantly within the cages, is less severe than anticipated because of the preferential location of CO_2 in the window regions. The deviations of IAST estimates from CBMC-simulated values increase with increasing pore occupancies.

Precisely analogous results are obtained for CO_2/CH_4 mixture adsorption in DDR, determined from two different CBMC campaigns; see Figure 9b. The CBMC-simulated S_{ads} values for the two sets of campaigns are not uniquely related to Φ, as is anticipated by the IAST; the non-unique $S_{ads} - \Phi$ characteristics are quantitatively captured by the RAST. As pore saturation conditions are approached, the IAST predictions of selectivities become increasingly optimistic.

2.6. Preferential Location of CO_2 within Pockets of AFX and MOR. Earlier works have shown that AFX zeolite is particularly effective for CO_2 capture applications.[70−72] Figure 10a shows snapshots for adsorption of the binary mixture of CO_2 and CH_4. In one unit cell of AFX, there are four 490 Å^3-sized cages, connected to four small pockets each of 98 Å^3. The 8-ring windows separating two cages are 3.44 Å × 3.88 Å in size. Guests such as CH_4, N_2, or H_2 are preferentially located within the cages. The competition experienced by CH_4, N_2, or H_2 from coadsorption with CO_2 should be expected to be significantly lowered because the window regions and the small pockets are preferred locations for CO_2.[67,70,71,73] Consequently, the IAST should be expected to overestimate the CO_2/CH_4 selectivity. The CBMC data for CO_2/CH_4 mixture adsorption in AFX confirms this expectation; see Figure 11a. Figure 11a also shows that the IAST overestimates the CO_2/CH_4 selectivity values in MOR zeolite because CO_2 gets firmly ensconced in the side pockets (cf. snapshots in Figure 10b), far removed from the CH_4 partners that preferentially reside in the main 12-ring 1D channels.

The segregation between CO_2 and its partners in MOR also results in selectivity reversals. Figure 11b shows CBMC data for $CO_2(1)/C_3H_8(2)$ mixture adsorption in all-silica MOR

Figure 10. (a) Snapshots showing the location of guest molecules for $CO_2(1)/CH_4(2)$ mixture adsorption in AFX zeolite at 300 K. (b) Snapshots showing the location of guest molecules for $CO_2(1)/C_3H_8(2)$ mixture adsorption in MOR zeolite at 300 K.
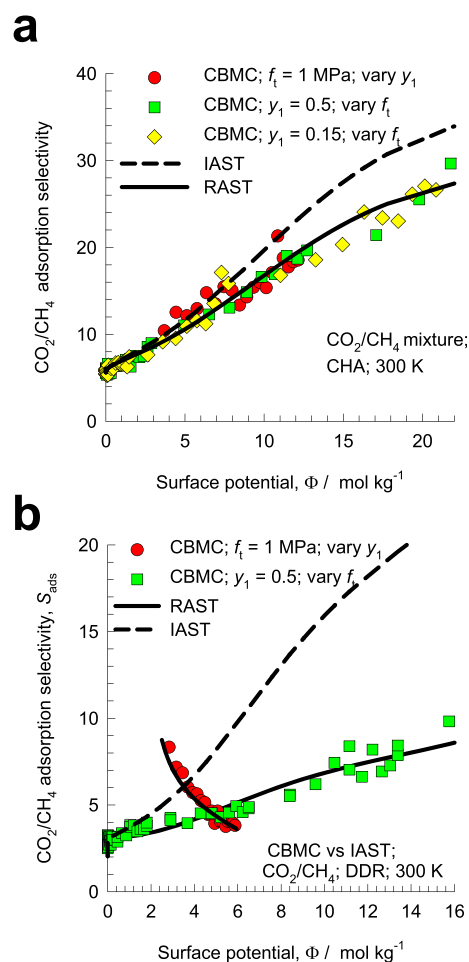
Figure 9. (a) CBMC data for adsorption selectivity S_{ads} for $CO_2(1)/CH_4(2)$ mixture adsorption in CHA zeolite, determined for three different campaigns: (i) constant composition $y_1 = 0.5$ with varying $f_t = f_1 + f_2$, (ii) constant composition $y_1 = 0.15$ with varying f_t, and (iii) $f_t = 1$ MPa with varying y_1. (b) CBMC data for adsorption selectivity S_{ads} for $CO_2(1)/CH_4(2)$ mixture adsorption in DDR, determined for two different campaigns: (i) constant composition $y_1 = 0.5$ with varying f_t and (ii) $f_t = 1$ MPa with varying composition y_1. The x-axes represent the surface potential Φ. The CBMC-simulated values (indicated by symbols) are compared with RAST (continuous solid lines) and IAST (dashed lines) estimates. All calculation details and input data are provided in the Supporting Information accompanying this publication.

zeolite for a campaign in which the total fluid phase fugacity f_t = 40 kPa and the bulk fluid phase mixture composition $y_1 = f_1/f_t$ is varied. For $y_1 < 0.6$, $S_{ads} > 1$, and the selectivity is in favor of CO_2. The CBMC simulations show that the adsorption selectivity S_{ads} is increasingly lowered below unity, i.e., in favor of alkane, with increasing proportion of CO_2 in the bulk gas phase. The IAST anticipates S_{ads} to be virtually independent of y_1 and does not anticipate the selectivity reversal phenomena. Experimental evidence is available for such selectivity reversals, which require the use of the RAST for quantification.[48,50]

2.7. Hydrogen Bonding in Water/Alcohol Mixtures. For water/alcohol mixture adsorption in zeolites and MOFs, the manifestation of hydrogen bonding between water and alcohol molecules can be demonstrated by sampling the spatial locations of the guest molecules to determine the O····H distances of various pairs of molecular distances. For water(1)/ethanol(2) mixture adsorption in DDR zeolite at 300 K, the
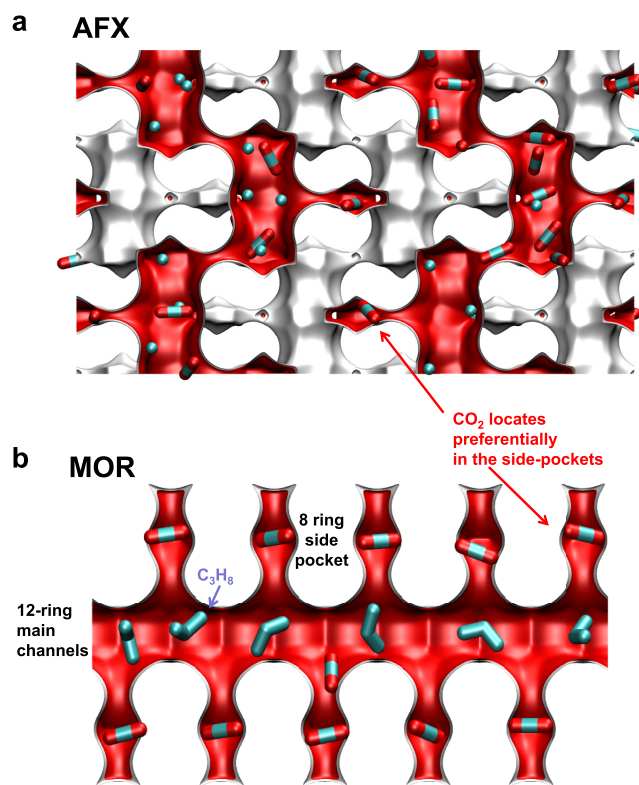
RDFs of O····H distances for water−water, water−ethanol, and ethanol−ethanol pairs are shown in Figure 12. We note that the first peaks in the RDFs occur at a distance less than 2 Å, which is characteristic of hydrogen bonding.[74,75] The heights of the first peaks are a direct reflection of the degree of hydrogen bonding between the molecular pairs. The degree of H-bonding between water−ethanol pairs is significantly larger, by about an order of magnitude, than for water−water and ethanol−ethanol pairs.

Figure 13a presents CBMC data on the ethanol/water selectivity in DDR for mixtures in which the partial fugacities are maintained equal for both guests, i.e., $f_1 = f_2$. With increasing values of the surface potential, the selectivity increasingly favors water adsorption due to its smaller size. For $\Phi \approx 10$ mol kg^{-1}, corresponding to a pore occupancy $\theta \approx$ 0.9, the mixture adsorption is water-selective. Although the IAST calculations (dashed lines) correctly anticipate the selectivity reversal phenomenon, the quantitative agreement of IAST estimates with CBMC data is poor. For $\Phi < 10$ mol kg^{-1}, the IAST overestimates S_{ads} due to enhanced water uptake resulting from molecular clustering. A further, distinct consequence of molecular clustering effects induced by hydrogen bonding is that the effective size difference between the guest molecules is reduced. Consequently, entropy effects are moderated by clustering phenomena. The IAST that does not account for clustering anticipates an exaggerated influence of entropy effects. In other words, for $\Phi > 10$ mol kg^{-1}, cluster formation tends to moderate entropy effects, and the IAST anticipates stronger water selectivity than found in CBMC simulations.
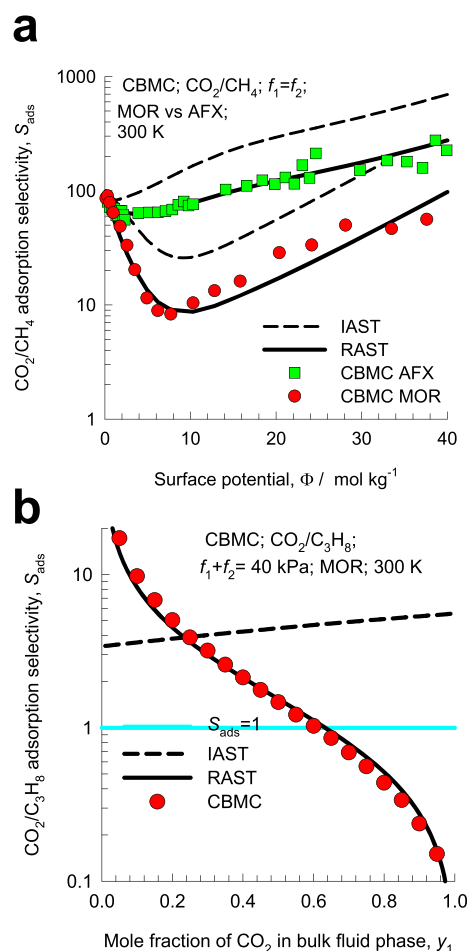
Figure 11. (a) CBMC simulation data on the adsorption selectivity S_{ads} for equimolar $f_1 = f_2$ $CO_2(1)/CH_4(2)$ mixture adsorption in AFX and MOR zeolites at 300 K, plotted as a function of the surface potential Φ. (b) CBMC simulation data on the adsorption selectivity for $CO_2(1)/C_3H_8(2)$ mixture adsorption in MOR zeolite at 300 K. The total fluid phase fugacity is $f_t = 1$ MPa, and the composition y_1 is varied. In panels (a) and (b), the CBMC-simulated values (indicated by symbols) are compared with RAST (continuous solid lines) and IAST (dashed lines) estimates. All calculation details and input data are provided in the Supporting Information accompanying this publication.

Figure 13b presents CBMC data for ethanol/water selectivity in DDR zeolite for a campaign in which the bulk fluid composition is varied while holding the total bulk mixture fugacity constant at $f_t = 10$ kPa. The CBMC data show that for water-rich mixtures, $y_1 > 0.5$, the adsorption is ethanol-selective; this is desired of adsorbents, say, in recovery of bioethanol from fermentation broths. However, for feed mixtures that are richer in ethanol, $y_1 < 0.5$, the adsorption is water-selective; this is a desirable feature, say, for use of DDR in membrane constructs for water-selective pervapora-tion processes.[76] The IAST (dashed line) anticipates ethanol-selective adsorption over the entire range of compositions y_1.

The combined set of component loadings in the two CBMC campaigns was used to determine the set of Margules parameters $A_{12} = -5.325$, $A_{21} = -1.665$, and $C = 1.868$ kg mol^{-1} to quantify the non-idealities. Figure 13c presents the RAST calculations of the activity coefficients for equimolar water/ethanol mixtures with varying f_t. As the surface potential $\Phi \rightarrow 0$, both activity coefficients tend to unity $\gamma_1 \rightarrow 1$, $\gamma_2 \rightarrow 1$,
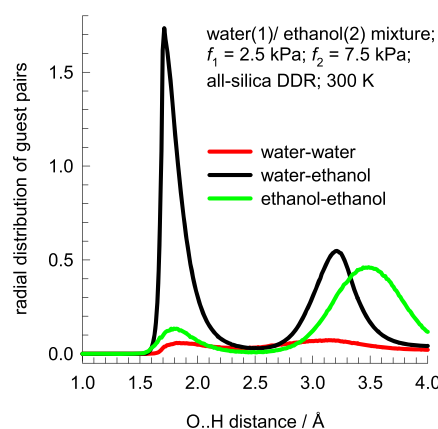

Figure 12. RDF of O····H distances for molecular pairs of water(1)/ethanol(2) mixture adsorption in DDR zeolite at 300 K. The partial fugacities of components 1 and 2 are $f_1 = 2.5$ kPa and $f_2 = 7.5$ kPa. The magnitudes of the first peaks are a direct reflection of the degree of hydrogen bonding between the molecular pairs.

as is expected in the Henry regime. The water activity coefficient exhibits a deep minimum for $0.01 < \Phi < 10$ mol kg^{-1}; under these conditions, there is significant enhancement in the water ingress that is caused by hydrogen bonding. With increasing pore occupancy, there is a monotonous decrease in the activity coefficient of ethanol below unity.

Figure 13c presents the activity coefficients for the campaign in which $f_t = 10$ kPa and the bulk fluid mixture composition is varied. In this campaign, the variation of the surface potential is minimal and $\Phi \approx 7$ mol kg^{-1}. Both activity coefficients are strongly dependent on the composition of the adsorbed phase mixture, x_1, and satisfy the requirement $x_i \rightarrow 1$; $\gamma_i \rightarrow 1$. The use of the RAST is essential for quantitative modeling the selectivity reversals observed in Figure 13a,b.

Precisely analogous results are obtained for water/alcohol mixture adsorption in CHA; see Figures S36−S38. The adsorption of alcohol-rich feed mixtures in CHA is water-selective; therefore, CHA membranes are used for the purification of alcohols by membrane pervaporation because diffusion through 3.8 Å × 4.2 Å 8-ring windows of CHA also favors water.[29,75,77−79]

2.8. Segregated Adsorption Due to the Selective Size Exclusion of Guest Molecules. One scenario in which it is evident that the mandate of homogeneous distribution of adsorbates is not fulfilled is the one in which one of the guest molecules is effectively excluded from the pore space on the basis of molecular size. We discuss below three examples of mixture separations exploiting size exclusion; in all these cases, CBMC simulations of mixture adsorption are not feasible.

For reducing the nitrogen content of natural gas, consisting predominantly of CH_4, one practical solution is to choose materials such as Ba-ETS-4 (ETS = Engelhard titano-silicate; ETS-4 is also named as CTS-1 = contracted titano-silicate-1) with pore size ≈ 3.7 Å so as to effectively exclude the spherical CH_4 molecule (3.7 Å) while allowing entry for the pencil-like nitrogen molecule (4.4 Å × 3.3 Å).[80−84] The experimental data of Bhadra[85] for the binary mixture adsorption equilibrium of CH_4/N_2 mixtures in Ba-ETS-4 demonstrate the failure of the IAST due to the segregated nature of adsorption.[86]

For C_3H_6/C_3H_8 mixture separations, a potent strategy is to employ NbOFFIVE-1-Ni (KAUST-7)[87] or Co-gallate,[88] which almost completely excludes the saturated alkane from the
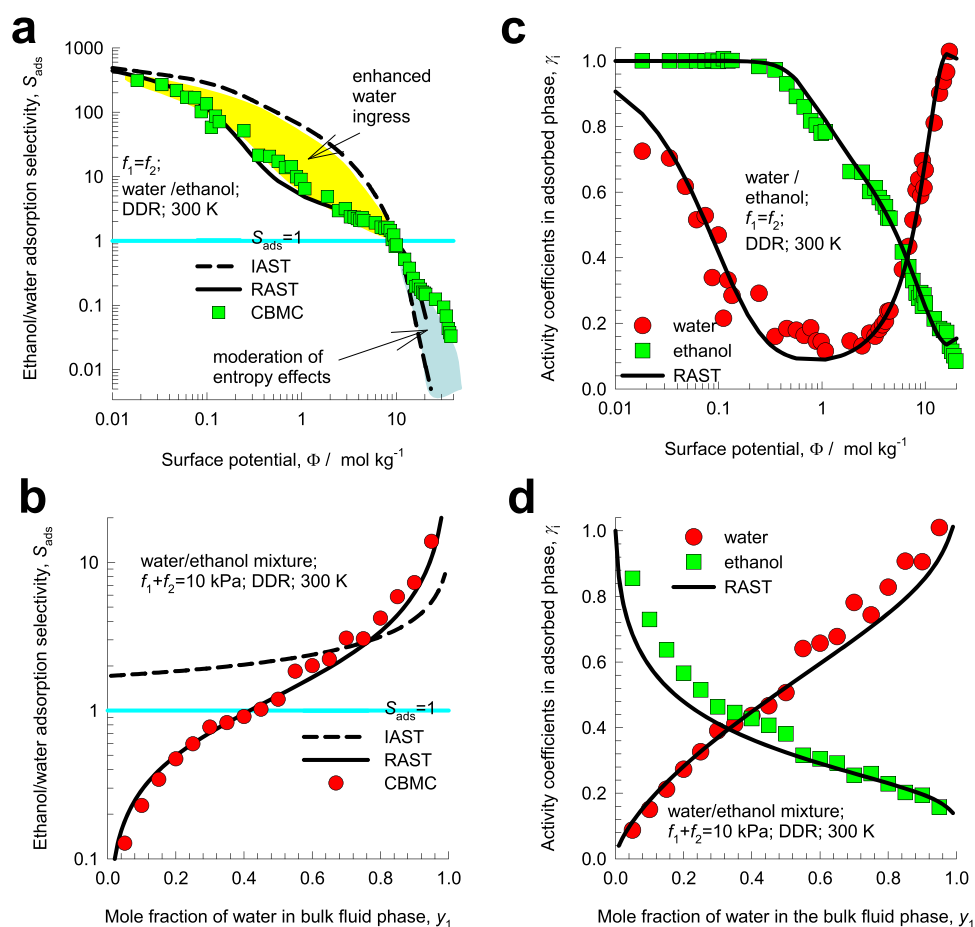
Figure 13. (a, b) CBMC simulation data for the ethanol/water selectivity S_{ads} for water(1)/ethanol(2) mixture adsorption in DDR at 300 K for two different campaigns. (a) In this campaign, the total fugacity f_t is varied, maintaining equal partial fugacities, $f_1 = f_2$, in the bulk fluid phase mixture. (b) In the second campaign, the total bulk fluid phase fugacity $f_t = f_1 + f_2 = 10$ kPa; the water composition in the bulk fluid mixture, y_1, is varied from 0 to 1. The CBMC-simulated values (indicated by symbols) are compared with RAST (continuous solid lines) and IAST (dashed lines) estimates. (c, d) RAST calculations of the activity coefficients, using fitted Margules parameters, for the two campaigns shown in panels (a) and (b). All calculation details and input data are provided in the Supporting Information accompanying this publication.

pores. For C_2H_4/C_2H_6 separations, near total exclusion of C_2H_6 is achieved by use of an ultramicroporous metal−organic framework UTSA-280 $[Ca(C_4O_4)(H_2O)]$, which possesses rigid one-dimensional channels.[14] The 1D channels are of a similar size to C_2H_4 molecules (all of atoms of which lie on the same plane) but, owing to the size, shape, and rigidity of the pores, practically exclude the C_2H_6. The applicability of the IAST to describe the mixture adsorption equilibrium for the aforementioned MOFs for alkene/alkane separations is clearly open to question.

3. CONCLUSIONS

The derivation of the IAST is based on two tenets: (i) homogeneous distribution of guest adsorbates in the pore space, allowing for equitable competition for the occupation of adsorption sites, and (ii) the surface area occupied by a guest molecule in the mixture that is essentially the same as for unary adsorption, implying no occurrence of clustering with partners. An important implication of the IAST is that the adsorption selectivity for the $i−j$ pair, $S_{ads,\,ij}$, is uniquely determined by the surface potential Φ, irrespective of the mixture composition and the presence of additional partners in the mixture. CBMC simulations of mixture adsorption in a wide variety of host

materials have been used to investigate and highlight scenarios in which the IAST tenets are violated.

(1) For the adsorption of CO_2-bearing mixtures, an inhomogeneous distribution of adsorbates is engendered due to congregation of CO_2 around the extra-framework cations in zeolites and exposed "open" charged metal sites of MOFs. Due to the inhomogeneous distribution of adsorbates, the partner molecules endure a reduced degree of competition with CO_2 than is presumed in the IAST. Consequently, the IAST generally tends to anticipate a higher selectivity of CO_2 with respect to partner species. The IAST also fails to anticipate reversals in the selectivity of CO_2-bearing mixtures of varying composition.

(2) For the adsorption of CO_2-bearing mixtures in cage-type zeolites such as CHA and DDR, the CO_2 molecules prefer to perch at the window regions; partner molecules such as CH_4 prefer to locate within the cages and enjoy reduced competition with partner CO_2 molecules. The IAST estimates of S_{ads} are overly optimistic. The preferential location of CO_2 within the side pockets of zeolites MOR and AFX leads to quantitative failure of the IAST for analogous regions. In severe cases, such as for CO_2/C_3H_8 adsorption in MOR, the IAST fails to

anticipate selectivity reversals; such failure has been confirmed by experiments.[48]

(3) The IAST mandate of homogeneous distribution of guest adsorbates is clearly violated for MOFs and zeolites that rely on the principle of size exclusion to enable separations.

(4) For separations of linear and branched alkanes using MFI zeolite, thermodynamic non-ideality effects arise due to the preferential location of the branched alkanes at the channel intersections that offer more "leg room". Aromatic molecules such as benzene also prefer to locate at the intersections, and consequently, the IAST estimates of component loadings and selectivities of adsorption of benzene/alkene and benzene/alkane mixtures are not of acceptable accuracy.

(5) For water/ethanol adsorption, molecular clustering occurs due to strong hydrogen bonding between water and ethanol. The IAST fails to provide quantitative predictions of selectivities for two separate reasons depending on the value of the surface potential Φ and pore occupancy θ. At relatively low values of Φ, water/ethanol clusters tend to increase the uptake of water, far in excess of the values anticipated by the IAST. Consequently, the IAST overestimates the ethanol/water selectivity. For large values of Φ, close to pore saturation, the occurrence of water/ethanol clusters has the effect of moderating entropy effects that normally favor the smaller water molecule with the higher saturation capacity. The IAST overestimates entropy effects and anticipates a higher degree of water selectivity than found in the CBMC simulations. The IAST does not also anticipate reversals that favor water in ethanol-rich mixtures.

(6) For quantification of non-ideality effects, activity coefficients γ_i need to be introduced as shown in eq 10. While the γ_i can be backed out from CBMC data on mixture adsorption, there are no reliable procedures for estimating these *a priori*. Streb and Mazzotti[40,41] discuss a procedure for the estimation of the RAST model parameters from cyclic experiments for CO_2/CH_4 mixture adsorption in 13X zeolite.

■ ASSOCIATED CONTENT

Ⓢ Supporting Information

The Supporting Information is available free of charge at https://pubs.acs.org/doi/10.1021/acsomega.1c02136.

Structural details of zeolites and MOFs, details of the CBMC simulation methodology, details of the IAST and Real Adsorbed Solution Theory (RAST) calculations for mixture adsorption equilibrium, unary isotherm fits for all the guest/host combinations, Margules and Wilson parameter fits for thermodynamic non-idealities, and plots of CBMC simulation data and comparisons with IAST/RAST estimates for all guest/host combinations (PDF)

■ AUTHOR INFORMATION

Corresponding Author

Rajamani Krishna − *Van't Hoff Institute for Molecular Sciences, University of Amsterdam, 1098 XH Amsterdam, The Netherlands;* ⓞ orcid.org/0000-0002-4784-8530; Email: r.krishna@contact.uva.nl

Author

Jasper M. van Baten − *Van't Hoff Institute for Molecular Sciences, University of Amsterdam, 1098 XH Amsterdam, The Netherlands*

Complete contact information is available at:
https://pubs.acs.org/10.1021/acsomega.1c02136

Notes

The authors declare no competing financial interest.

■ NOMENCLATURE

Latin alphabet

A	surface area per kg of framework, $m^2\ kg^{-1}$
A_{12}, A_{21}	Margules parameters, dimensionless
C	constant used in eq 14, $kg\ mol^{-1}$
f_i	partial fugacity of species i, Pa
f_t	total fugacity of the bulk fluid mixture, Pa
G^{excess}	excess Gibbs free energy, $J\ mol^{-1}$
n	number of species in the mixture, dimensionless
P_i^0	sorption pressure, Pa
q_i	molar loading of species i, $mol\ kg^{-1}$
$q_i^0(f)$	pure component adsorption isotherm for i, $mol\ kg^{-1}$
q_t	total molar loading of the mixture, $mol\ kg^{-1}$
$q_{sat,\ mix}$	saturation capacity of the mixture, $mol\ kg^{-1}$
R	gas constant, $8.314\ J\ mol^{-1}\ K^{-1}$
S_{ads}	adsorption selectivity, dimensionless
T	absolute temperature, K
x_i	mole fraction of species i in the adsorbed phase, dimensionless
y_i	mole fraction of species i in the bulk fluid mixture, dimensionless

Greek alphabet

γ_i	activity coefficient of component i in the adsorbed phase, dimensionless
θ	fractional occupancy, dimensionless
Θ_i	loading of species i, molecules per unit cell
π	spreading pressure, $N\ m^{-1}$
Φ	surface potential, $mol\ kg^{-1}$

Subscripts

i,j	components in mixture
t	referring to the total mixture
sat	referring to saturation con

Superscripts

0	referring to pure component loading
excess	referring to excess parameter

■ REFERENCES

(1) Myers, A. L.; Prausnitz, J. M. Thermodynamics of Mixed Gas Adsorption. *AIChE. J.* **1965**, *11*, 121−130.

(2) Walton, K. S.; Sholl, D. S. Predicting Multicomponent Adsorption: 50 years of the Ideal Adsorbed Solution Theory. *AIChE. J.* **2015**, *61*, 2757−2762.

(3) Xiang, S.; He, Y.; Zhang, Z.; Wu, H.; Zhou, W.; Krishna, R.; Chen, B. Microporous Metal-Organic Framework with Potential for Carbon Dioxide Capture at Ambient Conditions. *Nat. Commun.* **2012**, *3*, 954 http://dx.doi.org/doi:10.1038/ncomms1956.

(4) Krishna, R. Methodologies for Evaluation of Metal-Organic Frameworks in Separation Applications. *RSC Adv.* **2015**, *5*, 52269−52295.

(5) Krishna, R. Methodologies for Screening and Selection of Crystalline Microporous Materials in Mixture Separations. *Sep. Purif. Technol.* **2018**, *194*, 281−300.

(6) Herm, Z. R.; Swisher, J. A.; Smit, B.; Krishna, R.; Long, J. R. Metal-Organic Frameworks as Adsorbents for Hydrogen Purification and Pre-Combustion Carbon Dioxide Capture *J. Am. Chem. Soc.* **2011**, *133*, 5664−5667.

(7) Wu, H.; Yao, K.; Zhu, Y.; Li, B.; Shi, Z.; Krishna, R.; Li, J. Cu-TDPAT, an *rht*-type Dual-Functional Metal−Organic Framework Offering Significant Potential for Use in H₂ and Natural Gas Purification Processes Operating at High Pressures. *J. Phys. Chem. C* **2012**, *116*, 16609−16618.

(8) Yin, M. J.; Xiong, X. H.; Feng, X. F.; Xu, W. Y.; Krishna, R.; Luo, F. A Robust Cage-Based Metal−Organic Framework Showing Ultrahigh SO₂ Uptake for Efficient Removal of Trace SO₂ from SO₂/CO₂ and SO₂/CO₂/N₂ Mixtures. *Inorg. Chem.* **2021**, *60*, 3447−3451.

(9) Cui, X.; Chen, K.; Xing, H.; Yang, Q.; Krishna, R.; Bao, Z.; Wu, H.; Zhou, W.; Dong, X.; Han, Y.; Li, B.; Ren, Q.; Zaworotko, M. J.; Chen, B. Pore Chemistry and Size Control in Hybrid Porous Materials for Acetylene Capture from Ethylene. *Science* **2016**, *353*, 141−144.

(10) Li, B.; Cui, X.; O'Nolan, D.; Wen, H.-M.; Jiang, M.; Krishna, R.; Wu, H.; Lin, R.-B.; Chen, Y.-S.; Yuan, D.; Xing, H.; Zhou, W.; Ren, Q.; Qian, G.; Zaworotko, M. J.; Chen, B. An Ideal Molecular Sieve for Acetylene Removal from Ethylene with Record Selectivity and Productivity. *Adv. Mater.* **2017**, *29*, 1704210.

(11) Shen, J.; He, X.; Ke, T.; Krishna, R.; van Baten, J. M.; Chen, R.; Bao, Z.; Xing, H.; Dincă, M.; Zhang, Z.; Yang, Q.; Ren, Q. Simultaneous interlayer and intralayer space control in two-dimensional metal−organic frameworks for acetylene/ethylene separation. *Nat. Commun.* **2020**, *11*, 6259.

(12) Zhang, Y.; Hu, J.; Krishna, R.; Wang, L.; Yang, L.; Cui, X.; Duttwyler, S.; Xing, H. Rational design of microporous MOFs with anionic boron cluster functionality and cooperative dihydrogen binding sites for highly selective capture of acetylene. *Angew. Chem., Int. Ed.* **2020**, *59*, 17664−17669.

(13) Li, L.; Lin, R.-B.; Krishna, R.; Li, H.; Xiang, S.; Wu, H.; Li, J.; Zhou, W.; Chen, B. Ethane/ethylene Separation in a Metal-Organic Framework with Iron-Peroxo Sites. *Science* **2018**, *362*, 443−446.

(14) Lin, R.-B.; Li, L.; Zhou, H.-L.; Wu, H.; He, C.; Li, S.; Krishna, R.; Li, J.; Zhou, W.; Chen, B. Molecular Sieving of Ethylene from Ethane using a Rigid Metal-Organic Framework. *Nat. Mater.* **2018**, *17*, 1128−1133.

(15) Krishna, R. Screening Metal-Organic Frameworks for Mixture Separations in Fixed-Bed Adsorbers using a Combined Selectivity/Capacity Metric. *RSC Adv.* **2017**, *7*, 35724−35737.

(16) He, Y.; Krishna, R.; Chen, B. Metal-Organic Frameworks with Potential for Energy-Efficient Adsorptive Separation of Light Hydrocarbons. *Energy Environ. Sci.* **2012**, *5*, 9107−9120.

(17) Yang, H.; Wang, Y.; Krishna, R.; Jia, X.; Wang, Y.; Hong, A. N.; Dang, C.; Castillo, H. E.; Bu, X.; Feng, P. Pore-Space-Partition-Enabled Exceptional Ethane Uptake and Ethane-Selective Ethane−Ethylene Separation. *J. Am. Chem. Soc.* **2020**, *142*, 2222−2227.

(18) Peng, Y.-L.; Wang, T.; Jin, C.; Li, P.; Suepaul, S.; Beemer, G.; Chen, Y.; Krishna, R.; Cheng, P.; Pham, T.; Space, B.; Zaworotko, M. J.; Zhang, Z. A Robust Heterometallic Ultramicroporous MOF with Ultrahigh Selectivity for Propyne/Propylene Separation. *J. Mater. Chem. A* **2021**, *9*, 2850−2856.

(19) Peng, Y.-L.; He, C.; Pham, T.; Wang, T.; Li, P.; Krishna, R.; Forrest, K. A.; Hogan, A.; Suepaul, S.; Space, B.; Fang, M.; Chen, Y.; Zaworotko, M. J.; Li, J.; Li, L.; Zhang, Z.; Cheng, P.; Chen, B. Robust Microporous Metal-Organic Frameworks for Highly Efficient and Simultaneous Removal of Propyne and Propadiene from Propylene. *Angew. Chem., Int. Ed.* **2019**, *58*, 10209−10214.

(20) Li, L.; Wen, H.-M.; He, C.; Lin, R.-B.; Krishna, R.; Wu, H.; Zhou, W.; Li, J.; Li, B.; Chen, B. A Metal−Organic Framework with Suitable Pore Size and Specific Functional Site for Removal of Trace Propyne from Propylene. *Angew. Chem., Int. Ed.* **2018**, *57*, 15183−15188.

(21) Krishna, R. Metrics for Evaluation and Screening of Metal-Organic Frameworks for Applications in Mixture Separations. *ACS Omega* **2020**, *5*, 16987−17004.

(22) Banerjee, D.; Cairns, A. J.; Liu, J.; Krishna, R.; Thallapally, P. K.; Strachan, D. M. Potential of Metal-Organic Frameworks for Capture of Noble Gases. *Acc. Chem. Res.* **2015**, *48*, 211−219.

(23) Tao, Y.; Fan, Y.; Xu, Z.; Feng, X.; Krishna, R.; Luo, F. Boosting Selective Adsorption of Xe over Kr by Double-Accessible Open-Metal Site in Metal−Organic Framework: Experimental and Theoretical Research. *Inorg. Chem.* **2020**, *59*, 11793−11800.

(24) Motkuri, R. K.; Thallapally, P. K.; Annapureddy, H. V. R.; Dang, L.; Krishna, R.; Nune, S. K.; Fernandes, C. A.; Liu, J.; McGrail, B. P. Separation of Polar Compounds using a Flexible Metal-Organic Framework. *Chem. Commun.* **2015**, *51*, 8421−8424.

(25) Plessius, R.; Kromhout, R.; Ramos, A. L. D.; Ferbinteanu, M.; Mittelmeijer-Hazeleger, M. C.; Krishna, R.; Rothenberg, G.; Tanase, S. Highly Selective Water Adsorption in a Lanthanum Metal-Organic Framework. *Chem. − Eur. J.* **2014**, *20*, 7922−7925.

(26) He, C.-T.; Jiang, L.; Ye, Z.-M.; Krishna, R.; Zhong, Z.-S.; Liao, P.-Q.; Xu, J.; Ouyang, G.; Zhang, J.-P.; Chen, X.-M. Exceptional hydrophobicity of a large-pore metal-organic zeolite. *J. Am. Chem. Soc.* **2015**, *137*, 7217−7223.

(27) Zhang, K.; Lively, R. P.; Zhang, C.; Koros, W. J.; Chance, R. R. Investigating the Intrinsic Ethanol/Water Separation Capability of ZIF-8: An Adsorption and Diffusion Study. *J. Phys. Chem. C* **2013**, *117*, 7214−7225.

(28) Krishna, R.; van Baten, J. M. Screening Metal-Organic Frameworks for Separation of Pentane Isomers. *Phys. Chem. Chem. Phys.* **2017**, *19*, 8380−8387.

(29) Krishna, R. The Maxwell-Stefan Description of Mixture Diffusion in Nanoporous Crystalline Materials. *Microporous Mesoporous Mater.* **2014**, *185*, 30−50.

(30) Herm, Z. R.; Wiers, B. M.; Van Baten, J. M.; Hudson, M. R.; Zajdel, P.; Brown, C. M.; Maschiocchi, N.; Krishna, R.; Long, J. R. Separation of Hexane Isomers in a Metal-Organic Framework with Triangular Channels. *Science* **2013**, *340*, 960−964.

(31) Dubbeldam, D.; Krishna, R.; Calero, S.; Yazaydın, A. Ö. Computer-Assisted Screening of Ordered Crystalline Nanoporous Adsorbents for Separation of Alkane Isomers. *Angew. Chem., Int. Ed.* **2012**, *51*, 11867−11871.

(32) Yoon, J. W.; Lee, J. S.; Piburn, G. W.; Cho, K. H.; Jeon, K.; Lim, H.-K.; Kim, H.; Jun, C.-H.; Humphrey, S. M.; Krishna, R.; Chang, J.-S. Highly Selective Adsorption of p-Xylene over other C8 Aromatic Hydrocarbons by Co-CUK-1: A Combined Experimental and Theoretical Assessment. *Dalton Trans.* **2017**, *46*, 16096−16101.

(33) Krishna, R. Separating Mixtures by Exploiting Molecular Packing Effects in Microporous Materials. *Phys. Chem. Chem. Phys.* **2015**, *17*, 39−59.

(34) Torres-Knoop, A.; Krishna, R.; Dubbeldam, D. Separating Xylene Isomers by Commensurate Stacking of p-Xylene within Channels of MAF-X8. *Angew. Chem., Int. Ed.* **2014**, *53*, 7774−7778.

(35) Torres-Knoop, A.; Heinen, J.; Krishna, R.; Dubbeldam, D. Entropic Separation of Styrene/Ethylbenzene Mixtures by Exploitation of Subtle Differences in Molecular Configurations in Ordered Crystalline Nanoporous Adsorbents. *Langmuir* **2015**, *31*, 3771−3778.

(36) Mukherjee, S.; Joarder, B.; Desai, A. V.; Manna, B.; Krishna, R.; Ghosh, S. K. Exploiting Framework Flexibility of a Metal-Organic Framework for Selective Adsorption of Styrene over Ethylbenzene. *Inorg. Chem.* **2015**, *54*, 4403−4408.

(37) Wilkins, N. S.; Rajendran, A. Measurement of competitive CO₂ and N₂ adsorption on Zeolite 13X for post-combustion CO₂ capture. *Adsorption* **2019**, *25*, 115−133.

(38) Gholipour, F.; Mofarahi, M. Adsorption Equilibrium of Methane and Carbon Dioxide on Zeolite13X: Experimental and Thermodynamic Modeling. *J. Supercritical Fluids* **2016**, *111*, 47−54.

(39) Hefti, M.; Marx, D.; Joss, L.; Mazzotti, M. Adsorption Equilibrium of Binary Mixtures of Carbon Dioxide and Nitrogen on Zeolites ZSM-5 and 13X. *Microporous Mesoporous Mater.* **2015**, *215*, 215−228.

(40) Streb, A.; Mazzotti, M. Adsorption for efficient low carbon hydrogen production: part 1—adsorption equilibrium and break-through studies for $H_2/CO_2/CH_4$ on zeolite 13X. *Adsorption* **2021**, *27*, 541−558.

(41) Streb, A.; Mazzotti, M. Adsorption for efficient low carbon hydrogen production: part 2—Cyclic experiments and model predictions. *Adsorption* **2021**, *27*, 559−575.

(42) Costa, E.; Calleja, G.; Jimenez, A.; Pau, J. Adsorption Equilibrium of Ethylene, Propane, Propylene, Carbon Dioxide, and Their Mixtures in 13X Zeolite. *J. Chem. Eng. Data* **1991**, *36*, 218−224.

(43) Siperstein, F. R.; Myers, A. L. Mixed-Gas Adsorption. *AIChE. J.* **2001**, *47*, 1141−1159.

(44) Calleja, G.; Pau, J.; Calles, J. A. Pure and Multicomponent Adsorption Equilibrium of Carbon Dioxide, Ethylene, and Propane on ZSM-5 Zeolites with Different Si/Al Ratios. *J. Chem. Eng. Data* **1998**, *43*, 994−1003.

(45) Basmadjian, D.; Hsieh, S. T. Isothermal Column Sorption of Ethylene-Carbon Dioxide Mixtures with Azeotropic Behaviour. *Can. J. Chem. Eng.* **1980**, *58*, 185−189.

(46) van Zandvoort, I.; Ras, E.-J.; de Graaf, R.; Krishna, R. Using Transient Breakthrough Experiments for Screening of Adsorbents for Separation of C_2H_4/CO_2 Mixtures *Sep. Purif. Technol.* **2020**, *241*, 116706.

(47) van Zandvoort, I.; van der Waal, J. K.; Ras, E.-J.; de Graaf, R.; Krishna, R. Highlighting non-idealities in C_2H_4/CO_2 mixture adsorption in 5A zeolite. *Sep. Purif. Technol.* **2019**, *227*, 115730.

(48) Talu, O.; Zwiebel, I. Multicomponent Adsorption Equilibria of Nonideal Mixtures. *AIChE. J.* **1986**, *32*, 1263−1276.

(49) Krishna, R.; Van Baten, J. M. Using Molecular Simulations to Unravel the Benefits of Characterizing Mixture Permeation in Microporous Membranes in Terms of the Spreading Pressure. *ACS Omega* **2020**, *5*, 32769−32780.

(50) Krishna, R.; Van Baten, J. M. Elucidation of Selectivity Reversals for Binary Mixture Adsorption in Microporous Adsorbents. *ACS Omega* **2020**, *5*, 9031−9040.

(51) Krishna, R.; Van Baten, J. M. Using Molecular Simulations for Elucidation of Thermodynamic Non-Idealities in Adsorption of CO_2-containing Mixtures in NaX Zeolite. *ACS Omega* **2020**, *5*, 20535−20542.

(52) Krishna, R.; Van Baten, J. M. Water/Alcohol Mixture Adsorption in Hydrophobic Materials: Enhanced Water Ingress caused by Hydrogen Bonding. *ACS Omega* **2020**, *5*, 28393−28402.

(53) Krishna, R. Elucidation and Characterization of Entropy Effects in Mixture Separations with Micro-porous Crystalline Adsorbents. *Sep. Purif. Technol.* **2019**, *215*, 227−241.

(54) Talu, O.; Myers, A. L. Rigorous Thermodynamic Treatment of Gas-Adsorption. *AIChE. J.* **1988**, *34*, 1887−1893.

(55) Krishna, R.; Van Baten, J. M. Investigating the Non-idealities in Adsorption of CO_2-bearing Mixtures in Cation-exchanged Zeolites. *Sep. Purif. Technol.* **2018**, *206*, 208−217.

(56) Sochard, S.; Fernandes, N.; Reneaume, J.-M. Modeling of Adsorption Isotherm of a Binary Mixture with Real Adsorbed Solution Theory and Nonrandom Two-Liquid Model. *AIChE. J.* **2010**, *56*, 3109−3119.

(57) Mittal, N.; Bai, P.; Siepmann, J. I.; Daoutidis, P.; Tsapatsis, M. Bioethanol Enrichment using Zeolite Membranes: Molecular Modeling, Conceptual Process Design and Techno-Economic Analysis. *J. Membr. Sci.* **2017**, *540*, 464−476.

(58) Cessford, N. F.; Seaton, N. A.; Düren, T. Evaluation of Ideal Adsorbed Solution Theory as a Tool for the Design of Metal-Organic Framework Materials. *Ind. Eng. Chem. Res.* **2012**, *51*, 4911−4921.

(59) Gamba, G.; Rota, R.; Storti, G.; Carr, S.; Morbidelli, M. Absorbed Solution Theory Models for Multicomponent Adsorption Equilibria. *AIChE. J.* **1989**, *35*, 959−966.

(60) Zhang, H.; Wang, S. Modeling Bisolute Adsorption of Aromatic Compounds Based on Adsorbed Solution Theories. *Environ. Sci. Technol.* **2017**, *51*, 5552−5562.

(61) Erto, A.; Lancia, A.; Musmarra, D. Real Adsorbed Solution Theory model for competitive multicomponent liquid adsorption onto granular activated carbon. *Microporous Mesoporous Mater.* **2012**, *154*, 45−50.

(62) Bartholdy, S.; Bjørner, M. G.; Solbraa, E.; Shapiro, A.; Kontogeorgis, G. M. Capabilities and Limitations of Predictive Engineering Theories for Multicomponent Adsorption. *Ind. Eng. Chem. Res.* **2013**, *52*, 11552−11563.

(63) Vlugt, T. J. H.; Zhu, W.; Kapteijn, F.; Moulijn, J. A.; Smit, B.; Krishna, R. Adsorption of linear and branched alkanes in the silicalite-1. *J. Am. Chem. Soc.* **1998**, *120*, 5599−5600.

(64) Vlugt, T. J. H.; Krishna, R.; Smit, B. Molecular Simulations of Adsorption Isotherms for Linear and Branched Alkanes and Their Mixtures in Silicalite. *J. Phys. Chem. B* **1999**, *103*, 1102−1118.

(65) Krishna, R.; Smit, B.; Calero, S. Entropy effects during sorption of alkanes in zeolites. *Chem. Soc. Rev.* **2002**, *31*, 185−194.

(66) Schenk, M.; Vidal, S. L.; Vlugt, T. J. H.; Smit, B.; Krishna, R. Separation of alkane isomers by exploiting entropy effects during adsorption on silicalite-1: A configurational-bias Monte Carlo simulation study. *Langmuir* **2001**, *17*, 1558−1570.

(67) Krishna, R.; van Baten, J. M. Segregation effects in adsorption of CO_2 containing mixtures and their consequences for separation selectivities in cage-type zeolites. *Sep. Purif. Technol.* **2008**, *61*, 414−423.

(68) Krishna, R.; van Baten, J. M. A molecular dynamics investigation of the diffusion characteristics of cavity-type zeolites with 8-ring windows. *Microporous Mesoporous Mater.* **2011**, *137*, 83−91.

(69) Krishna, R.; van Baten, J. M. Onsager coefficients for binary mixture diffusion in nanopores. *Chem. Eng. Sci.* **2008**, *63*, 3120−3140.

(70) Krishna, R.; van Baten, J. M. A comparison of the CO_2 capture characteristics of zeolites and metal-organic frameworks. *Sep. Purif. Technol.* **2012**, *87*, 120−126.

(71) Krishna, R.; van Baten, J. M. In silico screening of metal-organic frameworks in separation applications. *Phys. Chem. Chem. Phys.* **2011**, *13*, 10593−10616.

(72) Bui, M.; Adjiman, C. S.; Bardow, A.; Anthony, E. J.; Boston, A.; Brown, S.; Fennell, P. S.; Fuss, S.; Galindo, A.; Hackett, L. A.; Hallett, J. P.; Herzog, H. J.; Jackson, G.; Kemper, J.; Krevor, S.; Maitland, G. C.; Matuszewski, M.; Metcalfe, I. S.; Petit, C.; Puxty, G.; Reimer, J.; Reiner, D. M.; Rubin, E. S.; Scott, S. A.; Shah, N.; Smit, B.; Trusler, J. P. M.; Webley, P.; Wilcox, J.; Mac Dowell, N. Carbon capture and storage (CCS): the way forward. *Energy Environ. Sci.* **2018**, *11*, 1062−1176.

(73) Krishna, R.; van Baten, J. M. Investigating cluster formation in adsorption of CO_2, CH_4, and Ar in zeolites and metal organic frameworks at sub-critical temperatures. *Langmuir* **2010**, *26*, 3981−3992.

(74) Zhang, C.; Yang, X. Molecular dynamics simulation of ethanol/water mixtures for structure and diffusion properties. *Fluid Phase Equilib.* **2005**, *231*, 1−10.

(75) Krishna, R.; van Baten, J. M. Hydrogen Bonding Effects in Adsorption of Water-alcohol Mixtures in Zeolites and the Consequences for the Characteristics of the Maxwell-Stefan Diffusivities. *Langmuir* **2010**, *26*, 10854−10867.

(76) Kuhn, J.; Castillo-Sanchez, J. M.; Gascon, J.; Calero, S.; Dubbeldam, D.; Vlugt, T. J. H.; Kapteijn, F.; Gross, J. Adsorption and Diffusion of Water, Methanol, and Ethanol in All-Silica DD3R: Experiments and Simulation. *J. Phys. Chem. C* **2009**, *113*, 14290−14301.

(77) Hasegawa, Y.; Abe, C.; Nishioka, M.; Sato, K.; Nagase, T.; Hanaoka, T. Formation of high flux CHA-type zeolite membranes and

their application to the dehydration of alcohol solutions. *J. Membr. Sci.* **2010**, *364*, 318−324.

(78) Krishna, R.; van Baten, J. M. Highlighting Pitfalls in the Maxwell-Stefan Modeling of Water-Alcohol Mixture Permeation across Pervaporation Membranes. *J. Membr. Sci.* **2010**, *360*, 476−482.

(79) Krishna, R.; van Baten, J. M. Mutual slowing-down effects in mixture diffusion in zeolites. *J. Phys. Chem. C* **2010**, *114*, 13154−13156.

(80) Bhadra, S. J.; Farooq, S. Separation of MethaneNitrogen Mixture by Pressure Swing Adsorption for Natural Gas Upgrading. *Ind. Eng. Chem. Res.* **2011**, *50*, 14030−14045.

(81) Majumdar, B.; Bhadra, S. J.; Marathe, R. P.; Farooq, S. Adsorption and Diffusion of Methane and Nitrogen in Barium Exchanged ETS-4. *Ind. Eng. Chem. Res.* **2011**, *50*, 3021−3034.

(82) Jayaraman, A.; Hernandez-Maldonado, A. J.; Yang, R. T.; Chinn, D.; Munson, C. L.; Mohr, D. H. Clinoptilolites for Nitrogen/Methane Separation. *Chem. Eng. Sci.* **2004**, *59*, 2407−2417.

(83) Yang, R. T. *Adsorbents: Fundamentals and Applications*. John Wiley & Sons, Inc.: Hoboken, New Jersey, 2003; pp 1−410.

(84) Habgood, H. W. The Kinetics of Molecular Sieve Action. Sorption of Nitrogen-Methane Mixtures by Linde Molecular Sieve 4A. *Canad. J. Chem* **1958**, *36*, 1384−1397.

(85) Bhadra, S. J. *Methane-Nitrogen Separation by Pressure Swing Adsorption*. Ph.D. Dissertation, National University of Singapore, Singapore, 2007.

(86) Krishna, R.; van Baten, J. M.; Baur, R. Highlighting the Origins and Consequences of Thermodynamic Nonidealities in Mixture Separations using Zeolites and Metal-Organic Frameworks. *Microporous Mesoporous Mater.* **2018**, *267*, 274−292.

(87) Cadiau, A.; Adil, K.; Bhatt, P. M.; Belmabkhout, Y.; Eddaoudi, M. A Metal-Organic Framework−Based Splitter for Separating Propylene from Propane. *Science* **2016**, *353*, 137−140.

(88) Liang, B.; Zhang, X.; Xie, Y.; RB, L.; Krishna, R.; Cui, H.; Li, Z.; Shi, Y.; Wu, H.; Zhou, W.; Chen, B. An Ultramicroporous Metal−Organic Framework for High Sieving Separation of Propylene from Propane. *J. Am. Chem. Soc.* **2020**, *142*, 17995−17801.